
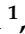





Article

The Effect of Germanium Additions on the Mechanical Properties of Zn-Mg-Al Alloys

Amar Dhoj Malla ^{1,*}, James Henley Sullivan ¹, David Jonathan Penney ¹, Elizabeth Sackett ¹, Robert Joseph Lancaster ¹ and Peter Barker ²

¹ Department of Materials, Swansea University, Swansea SA1 8EN, UK; j.h.sullivan@swansea.ac.uk (J.H.S.); d.penney@swansea.ac.uk (D.J.P.); e.sackett@swansea.ac.uk (E.S.); r.j.lancaster@swansea.ac.uk (R.J.L.)

² Tata Steel UK Limited, DE Shotton Works, Deeside CH5 2NH, UK; peter.d.barker@tatasteeleurope.com

* Correspondence: amar.malla@swansea.ac.uk

Abstract: In this investigation, 0.19–1.8 wt.% of Ge was introduced into a ternary Zn-Mg-Al alloy. The introduction of Ge had a significant impact on the microstructure, leading to the formation of Mg₂Ge. The area fraction of the eutectic phase diminished with increasing Ge additions. Small-scale test techniques were utilised to evaluate the mechanical properties due to the changes in microstructure. Zn-Mg-Al alloys were found to be inherently harder compared to standard hot-dip Zn-containing 0.2 wt.% Al. The hardness and strength of the Zn-Mg-Al alloys decreased with the increase in Ge additions.

Keywords: Zn-Mg-Al alloys; nano-indentation; small-scale testing; miniature technique; small punch tensile testing; vickers hardness

1. Introduction

Zinc (Zn) is one of the most popular metals on the planet. It is the fourth most used metal, with global demand of 13.77 Mt in 2018 [1]. Out of the total Zn consumed worldwide, approximately 50% is used in galvanising to protect steel from corrosion [1,2]. Zn-based alloys are also used in electronic systems, automotive parts, water taps and sanitary fittings, fashion goods, etc. [1]. Zn is also considered a new generation of biodegradable metal for biomedical implants; however, its clinical applications have been limited due to its inadequate mechanical properties [3]. Thus, a range of alloying elements such as magnesium (Mg), calcium (Ca), germanium (Ge) lithium (Li) and copper (Cu) have been used to improve its mechanical properties [4–10].

Hot-dip galvanised steels (HDGSs) are used in a wide variety of industries, from automotive and construction to white goods, due to their combined strength and corrosion resistance. HDGSs consist of an ultra-thin layer of Zn or a Zn alloy layer galvanised on either side of the steel substrate. These coating layers could easily be damaged under severe plastic deformation. HDGSs are shaped into a variety of desired forms and profiles via bending, stamping and pressing. Such processes can cause large deformations in the steel substrate and can also induce cracks in the hot-dip galvanised coating [11–13]. The efficiency of the protection provided by the coating is affected by the presence of these cracks. The propagation of induced cracks provides pathways for moisture and air to ingress into the bulk material, causing accelerated coating corrosion through galvanic effects and potentially premature steel corrosion. It is commercially desirable to minimise the formation of cracks on the coatings in order to prolong the life of HDGS products. Therefore, the mechanical properties and, most importantly, the formability of coating alloys are of paramount importance.

Zn with <0.2 wt. aluminium (Zn), binary zinc–aluminium (Zn-Al) (ZA) and ternary zinc–magnesium–aluminium (Zn-Mg-Al) (ZMA) are the three different commercially available hot-dip galvanising metallic coating alloys. Among the three, ZMA is considered



Citation: Malla, A.D.; Sullivan, J.H.; Penney, D.J.; Sackett, E.; Lancaster, R.J.; Barker, P. The Effect of Germanium Additions on the Mechanical Properties of Zn-Mg-Al Alloys. *Metals* **2024**, *14*, 820. <https://doi.org/10.3390/met14070820>

Academic Editor: Xiao-Wu Li

Received: 18 June 2024

Revised: 11 July 2024

Accepted: 15 July 2024

Published: 16 July 2024



Copyright: © 2024 by the authors. Licensee MDPI, Basel, Switzerland. This article is an open access article distributed under the terms and conditions of the Creative Commons Attribution (CC BY) license (<https://creativecommons.org/licenses/by/4.0/>).

to provide superior corrosion protection [14,15]. However, the addition of Mg and Al to Zn weakens the resulting mechanical properties, particularly resistance to plastic deformation [11,13,16]. Most previous ZMA studies focus on the microstructure and its corresponding corrosion performance [14,17–24]. The modification of the ZMA microstructure by quaternary elements targeting corrosion improvements has also been conducted [25–28]. Furthermore, the corrosion beneficiary effect of the quaternary addition of Germanium (Ge) and Bismuth (Bi) on the ZMA and Calcium (Ca) on the Zn has previously been reported [29–31].

In this study, the effect of Ge additions (0–1.8 wt.%) on the mechanical properties of Zn-Mg-Al (ZMA) was investigated. Furthermore, hot-dip galvanised Zn alloy (Galv Zn) (99.8 wt.% Zn–0.2 wt.% Al) was analysed as a benchmark alloy. To achieve this, a combination of small-scale testing techniques was employed. Vickers hardness and nano-indentation techniques were utilised to study the hardness whereas the small punch test was adopted to study the tensile behaviour.

2. Materials and Methods

2.1. Materials

HDG spelter (99.8 wt.% Zn–0.2 wt.% Al and saturated in iron (Fe)), (Galv Zn), was obtained from TATA Steel’s galvanising bath. The ZMA–Ge samples were manufactured in a controlled atmosphere of argon gas. ZMA (96.80% Zn, 1.6% Mg and 1.6% Al) ingots obtained from TATA Steel, Deeside, UK were induction heated to 650 °C in a crucible. Varying amounts of Ge were added to produce four different alloy compositions, as per Table 1. The alloys were further heated to 1000 °C and were allowed to air cool within the crucible. An IR thermometer Optris CT laser 3M pyrometer (Optris GmbH, Berlin, Germany) was used to measure the temperature on the alloy surface. The target compositions of the alloys under investigation are presented in Table 1.

Table 1. Target composition of the experimental samples.

Sample	Zn (wt.%)	Mg (wt.%)	Al (wt.%)	Ge (wt.%)
Galv Zn	99.80	-	0.20	-
ZMA–0 Ge	96.80	1.60	1.60	-
ZMA–0.19 Ge	96.61	1.59	1.59	0.19
ZMA–0.87 Ge	95.96	1.58	1.58	0.87
ZMA–1.80 Ge	98.05	1.57	1.57	1.80

2.2. Methods

2.2.1. Microstructural Analysis

The samples were mounted in non-conductive phenolic resin purchased from Met-prep Limited (Coventry, UK). The samples were ground using silicon carbide (SiC) paper (European P grade P2400 grit) followed by polishing using 1 µm diamond slurry. A Hitachi TM3000 Scanning Electron Microscope (SEM) with a Bruker Energy Dispersive X-ray Spectroscopy (EDS) module (Tokyo, Japan) was used to obtain images and conduct EDS analysis. The area fraction of different phases was calculated via image analysis of SEM images taken at 200× magnification. The image analysis software (Adobe Photoshop 2024, Adobe, San Josean, CA, USA) was spatially calibrated by setting a number of pixels to an already-known distance within the photographic image. Carbon tape was used to obtain an electrical connection. The area fraction of the alloys was determined via image analysis of five different SEM images.

2.2.2. Vickers Hardness

A Mitutoyo AVK-CL Vickers hardness tester was used to generate micro-hardness measurements of the samples. A load of 4.9 N was used to induce indents with a dwell time of 10 s. The diagonal indentation lengths were measured using a calibrated micrometre

attached to the eyepiece of the microscope. The samples were metallographically prepared prior to measurement as mentioned in Section 2.2.1.

2.2.3. Nano-Indentation

Nano-indentation is a long-established technique based on the interaction between the material and the indenter tip. In the last two decades, nano-indentation has been very popular in investigating the mechanical properties of materials because of its use of small test samples and small loading force. Oliver and Pharr developed an analysis method to calculate hardness and Young's modulus from the obtained load vs. displacement (P-h) curve [32–34]. Nano-indentation has been employed to measure the hardness and Young's modulus of thin films [35–37], microstructural phases [38,39] and bulk materials [40]. Although nano-indentation has been primarily implemented in the study of engineering materials, several investigations have explored its application in the study of biomaterials like bones as well as DNA [41,42].

The nano-indentation tests were performed using a Hysitron Ti 950 TriboIndenter (Bruker Corp., Billerica, MA, USA) machine equipped with a Berkovich diamond tip. The sample surfaces were prepared as detailed in Section 2.2.1 and finished with colloidal silica to give a 0.2 μm finish. The maximum indentation load was 500 μN with a dwell time of 5 s. Each indent was separated by 3 μm in order to prevent the possible intersecting of plastic deformation zones onto nearby indents.

2.2.4. Small Punch Tensile Test

The small punch tensile (SP) test consists of a miniature disc sample that is subjected to an applied compressive load via a hemispherical punch indenter onto the upper surface of the disc at a constant rate of displacement, forcing the disc through a receiving hole. A small punch test specimen and experimental set-up are presented schematically in Figure 1 [43].

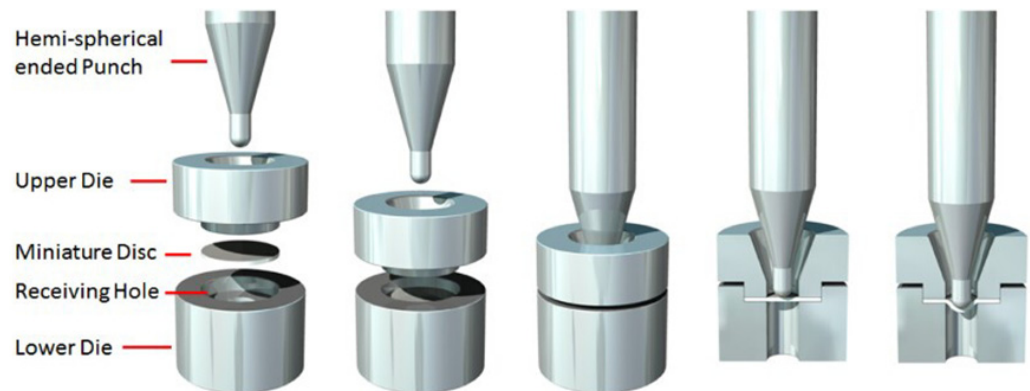


Figure 1. Schematic representation of the SP apparatus, disc retention and punch application reprinted from Ref [43].

The small punch technique uses small specimens measuring 8 mm in diameter, 500 μm in thickness ($\pm 5 \mu\text{m}$) and finished with a 1200 grit polishing cloth. During testing, the disc specimen is clamped between an upper and lower die set, where the load is applied through a 2.5 mm diameter indenter, forcing the material through a 4 mm diameter receiving hole. The test setup and relevant geometries are as per the EN standard for small punch testing [44]. Disc deflection is measured using a standard single linear variable displacement transducer (LVDT), which is placed below the specimen disc via a quartz rod. In addition, displacement values are also recorded directly from the machine cross-head. The experiments were carried out under a constant displacement rate of 0.5 $\text{mm}\cdot\text{min}^{-1}$ at room temperature.

Determination of Elastic–Plastic Transition Point (Yield Point, P_y)

The maximum force (P_m) and deflection at maximum force (u_m) can readily be obtained from the force–deflection (P - u) curve obtained from the SP test. The elastic–plastic transition point (yield point, P_y) is not clearly defined as yielding occurs successively in different areas of the specimen during the test [45]. Different methods of determining P_y are documented in the literature [45,46]. Here, the method proposed by Mao and Takahashi [47] was employed, where P_y is defined as the intersection of two tangents outlining the elastic regime and the plastic regime. Figure 2 illustrates the method used to define P_y along with the other properties derived from an SP test, such as maximum force (P_m), deflection at maximum force (u_m) and deflection at yield point (u_0).

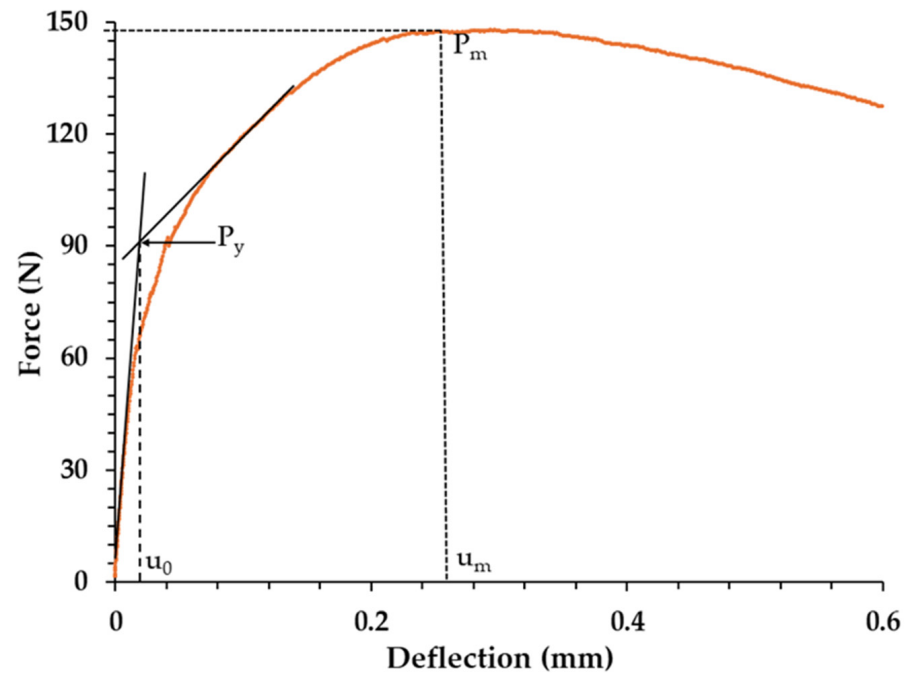


Figure 2. Force–deflection curve highlighting the different values obtained from an SP test, along with the method used to determine P_y .

3. Results

The microstructure images of Galv Zn and ZMA–0 Ge captured using a Scanning Electron Microscope (SEM) are presented in Figure 3A and 3B, respectively. The Galv Zn has a single-phase microstructure. ZMA–0 Ge comprises three different phases: primary zinc (Zn), binary eutectic and ternary eutectic. The binary eutectic phases are lamellar structures made up of intermetallic $MgZn_2$ and primary Zn phase, whilst ternary eutectic is made up of primary Zn, $MgZn_2$ and aluminium (Al) nodules. The effect of 0.19 wt.%–1.8 wt.% of germanium (Ge) additions to the ZMA microstructure is presented in Figure 3C–E. The additions resulted in the formation of a new phase within the microstructure, which was previously identified as magnesium germanide (Mg_2Ge) [30]. These newly formed Mg_2Ge due to Ge additions could be present in two different forms: plate-like structures as seen in ZMA–0.19 Ge (Figure 3C) and ZMA–0.87 Ge (Figure 3D) and hopper crystals as seen in ZMA–1.8 Ge (Figure 3E). This change in the morphology of Mg_2Ge could be due to the high affinity of Ge to Mg. In the lower Ge content samples, there is enough Mg present in the liquidus to form a fully plated-shaped Mg_2Ge phase whereas for the high Ge content sample (ZMA–1.8 Ge), there is not enough Mg available, thus leading to the formation of hopper crystals.

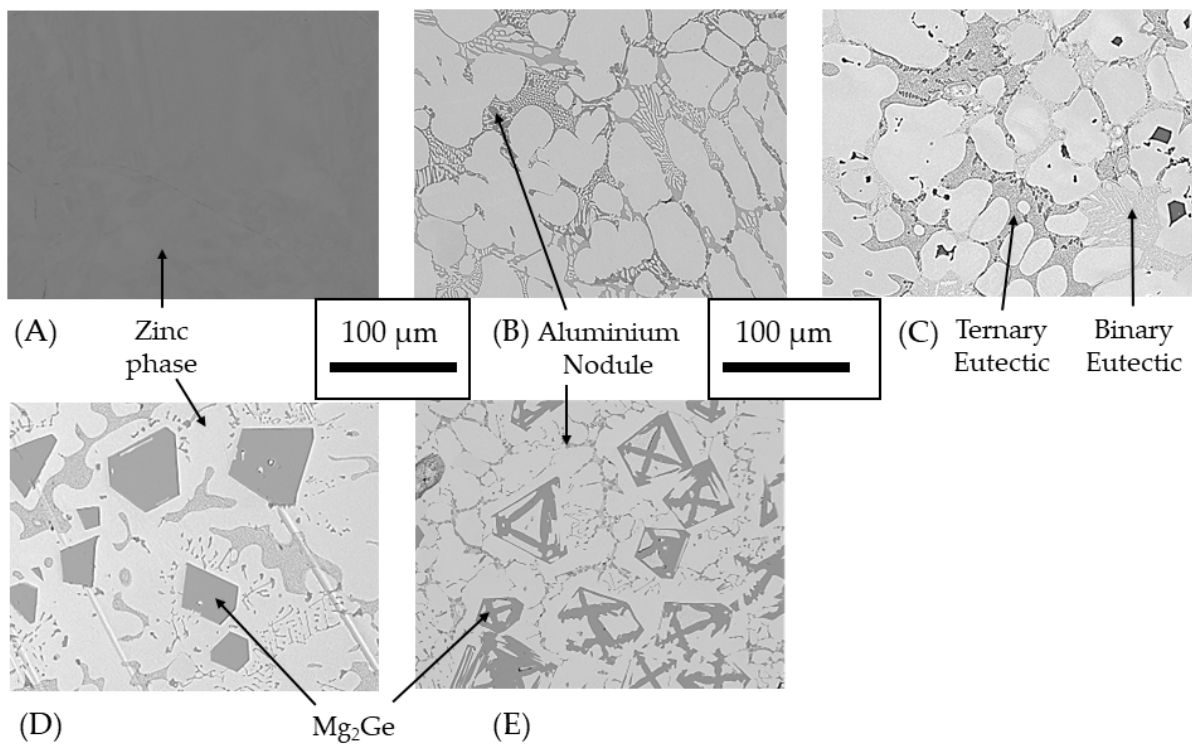


Figure 3. SEM images showing the microstructure of (A) Galv Zn (B) ZMA-0 Ge (C) ZMA-0.19 Ge (D) ZMA-0.87 Ge and (E) ZMA-1.8 Ge.

The average surface area fraction of different phases, calculated from three different areas of each of the alloys, is displayed in Table 2.

Table 2. Area fraction of phases present in the experimental samples.

Sample	Primary Zn (Surface Area %)	Eutectic (Surface Area %)	Mg ₂ Ge (Surface Area %)
Galv Zn	100	-	-
ZMA-0 Ge	65.52 ± 2.18	34.48 ± 1.92	-
ZMA-0.19 Ge	69.89 ± 6.21	28.54 ± 6.27	1.57 ± 0.07
ZMA-0.87 Ge	72.17 ± 0.45	23.23 ± 0.64	4.60 ± 0.22
ZMA-1.80 Ge	77.31 ± 5.67	8.41 ± 1.27	14.28 ± 6.84

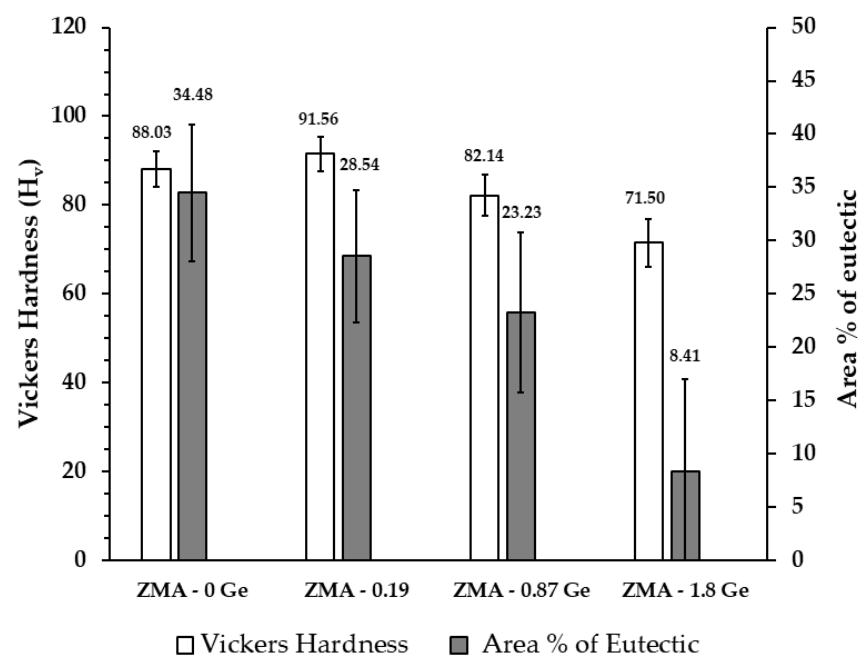
The surface area fraction of Galv Zn was 100% Zn phase. For ZMA-0 Ge, the surface area fraction for primary Zn was 65.52 ± 2.18% and the eutectic phase was 34.48 ± 1.92%. The percentage of the surface area covered by the Zn phase increased with the increase in Ge additions, i.e., 65.52 ± 2.18% for ZMA-0 Ge to 77.31 ± 5.67% for ZMA-1.8 Ge. Correspondingly, the percentage of the surface area made up of the eutectic phase decreased with the increase in Ge additions, i.e., 34.48 ± 1.92% for ZMA-0 Ge to 8.41 ± 1.27% for ZMA-1.8 Ge. Additionally, the percentage of the surface area made up by the Mg₂Ge increased with the increase in Ge additions from 1.57 ± 0.07% for ZMA-0.19 Ge to 14.28 ± 6.84% for ZMA-1.8 Ge.

The results of the Vickers hardness test are presented in Table 3. The errors shown are based on the standard deviation of 10 measurements. The results show that ZMA-0 Ge is inherently harder compared to Galv Zn. The H_v of ZMA-0 Ge (88.03 H_v) is 40% greater compared to Galv Zn (51.60 H_v).

Table 3. Vickers hardness (H_V) values measured for Galv Zn and ZMA–Ge alloys.

Sample	Vickers Hardness (H_V)
Galv Zn	51.60 ± 1.94
ZMA–0 Ge	88.03 ± 4.00
ZMA–0.19 Ge	91.56 ± 3.87
ZMA–0.87 Ge	82.14 ± 4.65
ZMA–1.80 Ge	71.50 ± 5.33

For ZMA–Ge alloys, the hardness decreased with an increase in Ge addition, except for 0.19 Ge addition where a similar H_V was observed. The result shows hardness in the order ZMA–1.8 Ge < ZMA–0.87 Ge < ZMA–0 Ge < ZMA–0.19 Ge. The relationship between the hardness (H_V) and the area % of the eutectic phase of ZMA–Ge alloys is presented in Figure 4.

**Figure 4.** Relationship between the hardness and the surface area % of the eutectic phase of ZMA–Ge alloys.

In Figure 4, except for ZMA–0.19 Ge, a direct relationship between the hardness (H_V) and surface area % of the eutectic phase is observed, i.e., H_V decreases with the decrease in area % of the eutectic phase.

The hardness of the experimental samples (Galv Zn and ZMA–Ge alloys) was further investigated using the nano-indentation technique. This permits the measurement of the hardness of primary Zn and eutectic phases individually. Since nanomechanical properties were being investigated, the two extremes of ZMA–0 Ge and ZMA–1.8 Ge along with Galv Zn were selected for analysis. The results are displayed in Figure 5.

The load–depth (P - h) curves obtained after the nano-indentation tests were divided into three different phases in accordance with the load shift. The first phase is the loading phase prior to the maximum indentation load being reached. During the loading process, elastic deformation is followed by plastic deformation. The second phase is where dwell occurs, where the maximum load is maintained. This dwell is presented as a short flat line at maximum load in Figure 5. The final phase is the unloading phase. The applied load is gradually lowered until it is entirely unloaded. The indentation deformation consists of elastic and plastic deformation during loading whereas it is pure elastic deformation during unloading [48].

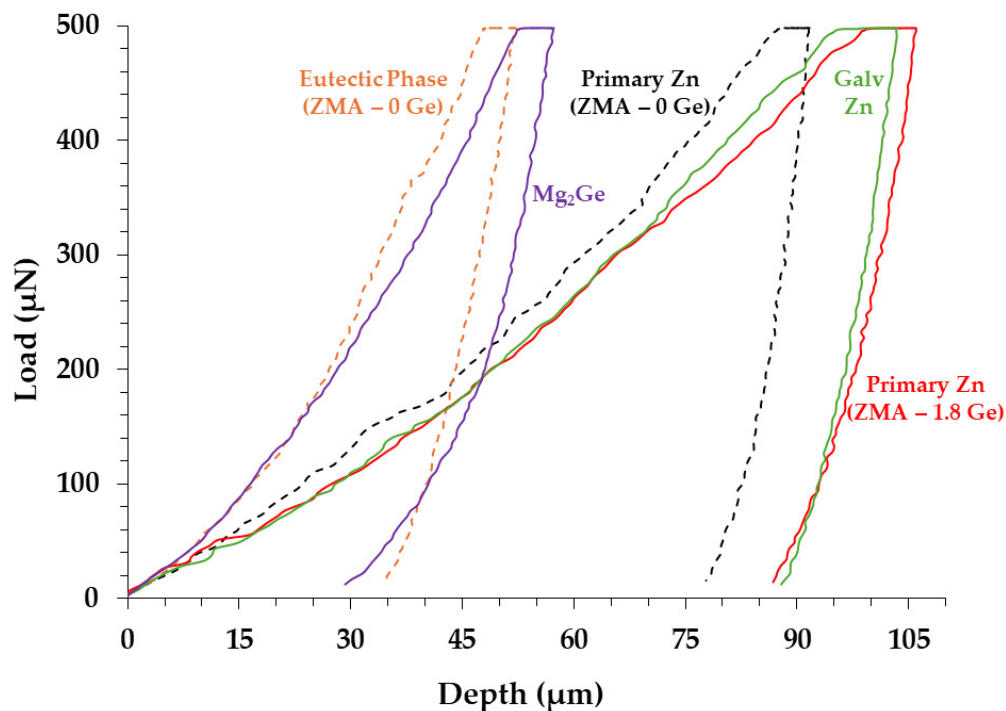


Figure 5. Load–depth (P-h) nano-indentation curves obtained for Galv Zn, ZMA-0 Ge and ZMA-1.8 Ge and Mg_2Ge .

Figure 5 demonstrates that the P-h curve of primary Zn of ZMA-0 Ge has shifted to the left relative to Galv Zn whose microstructure is 100% Zn phase. However, for the eutectic phase of ZMA-0 Ge, the shift of the P-h curve towards the left is significantly greater. In addition, an appreciable decrease in the depth of penetration and an increase in the slope of the loading phase is observed for the eutectic phase of ZMA-0 Ge. The shift of the P-h curve toward the left direction, accompanied by a decrease in the penetration depth and an increase in the slope of the loading curve indicates an increase in hardness for the eutectic phase compared to the Zn phase. The primary Zn phase of ZMA-1.8 Ge demonstrated a P-h curve similar to Galv Zn with a very small shift to the right. The P-h curve of Mg_2Ge was very similar and demonstrated similar characteristics to the eutectic phase of ZMA-0 Ge.

The reduced elastic modulus (E_r) and hardness (H) values obtained from the P-h curves are presented in Table 4. The unloading curves were analysed with the upper 10% and lower 70% disregarded for curve fitting to calculate hardness and reduced modulus values. The errors shown are based on the standard deviation of five measurements. The E_r for the Zn phase of Galv Zn, ZMA-0 Ge, the eutectic phase of ZMA-0 Ge and the Zn phase of ZMA-1.8 Ge and Mg_2Ge are 89.92 GPa, 113.02 GPa, 125.92 GPa, 78.07 GPa and 136.39 GPa, respectively. Similarly, the hardness (H) values for the Zn phase of Galv Zn, ZMA-0 Ge, the eutectic phase of ZMA-0 Ge, the Zn phase of ZMA-1.8 Ge and Mg_2Ge are 1.34 GPa, 1.96 GPa, 4.55 GPa, 1.65 GPa and 6.79 GPa, respectively.

Table 4. Reduced elastic modulus and hardness values obtained from nano-indentation tests on Galv Zn and ZMA-Ge alloys.

	Galv Zn	Primary Zn (ZMA-0 Ge)	Eutectic Phase (ZMA-0 Ge)	Primary Zn (ZMA-1.8 Ge)	Mg_2Ge
Reduced Elastic Modulus (E_r) (GPa)	89.92 ± 4.02	113.02 ± 2.46	125.91 ± 10.82	78.07 ± 6.37	136.39 ± 7.39
Hardness (H) (GPa)	1.34 ± 0.27	1.96 ± 2.46	4.55 ± 1.17	1.65 ± 0.15	6.79 ± 0.58

The experimental alloys were further characterised using the SP test. Force–deflection curves for the Galv Zn and ZMA–Ge alloys tested at room temperature under a displacement rate of $0.5 \text{ mm}\cdot\text{min}^{-1}$ are presented in Figure 6. A significant difference was observed between the responses of Galv Zn and ZMA–Ge alloys. The ZMA–Ge alloys' force–deflection curves displayed a steeper gradient in comparison to those of Galv Zn. For ZMA–Ge alloys, all of the force–deflection curves displayed similar characteristics; however, it was at the latter end of the experiment that differences could be identified where the curves shallowed. The shallowing of the gradient after P_m was attributed to the onset of cracking in the specimen and the alloys' damage tolerance. The characteristic points; maximum force (P_m), displacement at maximum force (u_m) and deflection at yield point (u_0) obtained from the force–deflection curves shown in Figure 6 are presented in Table 5.

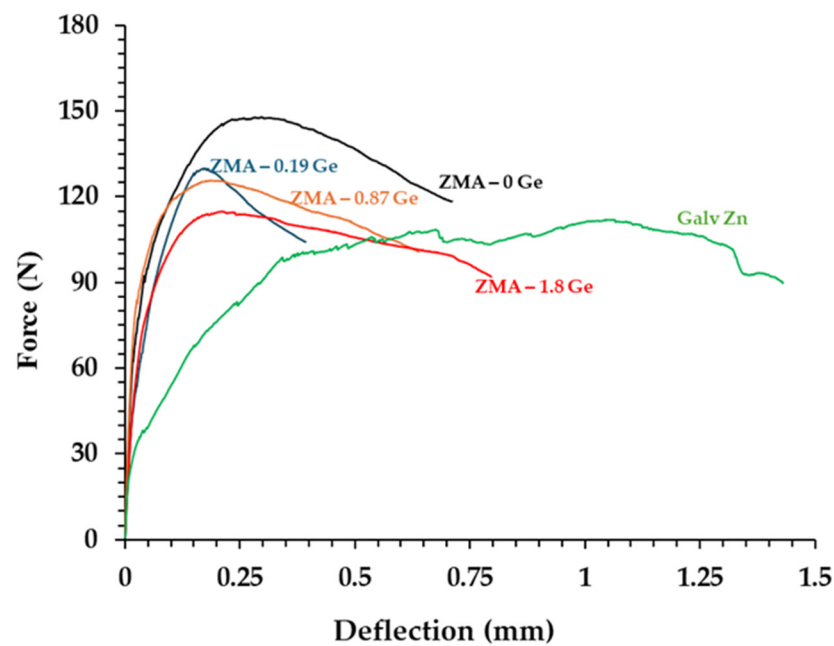


Figure 6. Force–deflection curves for the Galv Zn and ZMA–Ge alloys obtained after SP testing conducted at room temperature at a displacement rate of $0.5 \text{ mm}\cdot\text{min}^{-1}$.

Table 5. Properties derived from the SP test for Galv Zn and ZMA–Ge alloys.

Sample	P_m (N)	u_m (mm)	P_y (N)	u_0 (mm)	$u_m - u_0$ (mm)	Predicted σ_{UTS} (MPa)	Predicted σ_{ys} (MPa)
Galv Zn	112.20	1.04	25	0.02	1.02	136.5	168.4
ZMA–0 Ge	147.82	0.30	70	0.02	0.28	303.5	231.2
ZMA–0.19 Ge	130.04	0.17	78	0.01	0.16	421.6	242.4
ZMA–0.87 Ge	125.67	0.18	74	0.01	0.17	392.6	236.8
ZMA–1.8 Ge	114.84	0.21	73	0.02	0.19	327.0	239.6

When comparing the P_m values for the different materials, it is important to note that despite the ZMA–0 Ge composition appearing to achieve the highest P_m value, care should be taken when attempting to compare this behaviour with other test types. This is because, when correlating P_m to the more established ultimate tensile stress (σ_{UTS}) property found in uniaxial tensile testing, the empirical relationship also incorporates u_m into the calculation, as follows:

$$\sigma_{UTS} = \beta_1 \left(\frac{P_m}{t \cdot u_m} \right) + \beta_2 \quad (1)$$

where t is the specimen thickness and β_1 and β_2 are constants derived from linear regression. In previous research, Lancaster et al. [49] derived β_1 to be 0.22 and β_2 to be 89.74, as

determined through a series of SP and uniaxial tensile experiments performed on a number of established metallic materials. Using this equation, a predicted σ_{UTS} value can be derived, as displayed in Table 5. The predicted σ_{UTS} values show that the ZMA–0.19 Ge composition now exhibits the highest strength, corroborating with the findings from the Vickers Hardness tests.

Similar to the correlation defined for σ_{UTS} , predicted yield stress (σ_{ys}) can also be derived through the following equation:

$$\sigma_{ys} = \alpha_1 \left(\frac{P_y}{t^2} \right) + \alpha_2 \quad (2)$$

where α_1 and α_2 are constants again acquired from linear regression. As taken from the same source [49], $\alpha_1 = 349.1$ and $\alpha_2 = 133.5$. From these empirical calculations (as presented in Table 5), the predicted σ_{ys} values follow the same ordering as those established for σ_{UTS} , where the ZMA–0.19 Ge composition displays the highest yield properties, with the ZMA–0 Ge material performing the worst.

Although the H_v of ZMA–0 Ge and ZMA–0.19 Ge are similar in the limits of the confidence interval, here, the predicted tensile strength σ_{UTS} and σ_{ys} of ZMA–0.19 Ge are 38.90% and 4.84% higher, respectively, than ZMA–0 Ge. This is because σ_{UTS} is inversely proportional to u_m and σ_{ys} is directly proportional to P_y (Equations (1) and (2)). ZMA–0.19 Ge has the lowest u_m (0.17 mm) and the highest P_y (78 N) among the tested alloys. This could be due to a fine balance of large eutectic content and Mg_2Ge phases.

The formability of a material is associated with the plastic deformation region on a force–deflection curve, and it can be represented in terms of the difference between deflection at u_m and u_0 . The $u_m - u_0$ for all of the investigated materials is presented in Table 5. Among the tested alloys, Galv Zn demonstrated the best formability and outperformed all of the ZMA–Ge alloys. The ($u_m - u_0$) deflection of Galv Zn was ~4 times the ZMA–0 Ge. The Ge additions (ZMA–Ge alloys) further deteriorated the formability of ZMA–0 Ge. For example, the ($u_m - u_0$) deflection of ZMA–1.8 Ge (0.19 mm) was 32% lower compared to that of ZMA–0 Ge (0.28 mm).

4. Discussion

As shown in Table 1, the microhardness (H_v) of the Galv Zn increased with the addition of 1.6 wt.% Mg and 1.6 wt.% Al (ZMA–0 Ge) from 51.60 to 88.03. The addition of Mg and Al leads to the formation of eutectic phases; binary (Zn and $MgZn_2$) and ternary (Zn, $MgZn_2$ and Al) around the Zn phase (Figure 3). These eutectic phases behave as holding points and obstruct dislocation movement [50]. Therefore, more energy is required for dislocations to move to the adjacent phase, consequently disrupting the dislocation movement in a continuous slip plane.

The addition of 1.6 wt.% Mg & 1.6 wt.% Al (ZMA–0 Ge) also increased the nano hardness from 1.34 GPa of Galv Zn to 1.96 GPa for the Zn phase of ZMA–0 Ge. Though limited, there was some dissolution of Mg and Al into the primary zinc matrix. The solubility of Mg and Al zinc is presented in Table 6 [51,52]. The Mg and Al atoms present within the crystalline lattices of the Zn phase of ZMA–0 Ge interrupt the regularity of the crystal lattice. The movement of the dislocations is interrupted or prevented by these irregularities and therefore requires higher stress or thermal energy to overcome irregularities, consequently increasing the hardness.

Table 6. Solubility of magnesium and aluminium in zinc matrix.

Temperature	Mg (wt.%)	Al (wt.%)
RT	0.008	0.07

The microhardness of the ZMA–Ge alloys decreased as Ge addition increased (Table 1). This softening can be explained due to the changes in the microstructure. Due to the high

affinity of Ge to Mg, the addition of Ge led to the formation of the Mg_2Ge phase (Figure 3). As the addition of Ge increases, the area of eutectic phases decreases (Table 2), hence contributing to nanohardness softening.

Similarly, as more or most of Mg is trapped in the Mg_2Ge phase for ZMA–1.8 Ge, no or less Mg is present in the Zn matrix of ZMA–1.8 Ge; as a result, a significant reduction in the elastic modulus of the Zn phase in ZMA–1.8 Ge is observed compared to the Zn phase in ZMA–0 Ge.

The addition of Ge to the ZMA alloy led to a decrease in the hardness of the alloy as observed during the Vickers hardness test whereas the SP tests showed a decrease in the level of plastic deformation after P_m and thus the formability. The decrease in the hardness of the alloy observed during the Vickers hardness test could be due to the decrease in area % of the brittle eutectic phase with an increase in Ge concentration and also the indents covering more of the Zn matrix per unit area.

The SP tests showed a reduction in formability and this could be due to the substitution of intermetallic $MgZn_2$ by another intermetallic, Mg_2Ge , which could potentially act as a crack nucleator during the SP test. Furthermore, even in the alloy with the highest Ge content, ZMA–1.8 Ge, the eutectic phase is not entirely substituted and some eutectic phase is still present (Figure 3). This presence of the residual eutectic phase will influence the alloy's plasticity, as cracks have been shown to initiate in this brittle $MgZn_2$ phase [13]. Despite this, there was clear evidence that the presence of Ge led to an increase in the strength-based properties up to 0.19 wt.%. However, beyond this, both the σ_{ys} and σ_{UTS} values decreased with an increase in Ge wt.%, a behaviour that was also seen in the hardness results.

5. Conclusions

A combination of small-scale test techniques, the Vickers hardness test, the nano-indentation technique and the small punch tensile test, were used to investigate the mechanical properties of Galv Zn and ZMA–Ge alloys. Among the investigated alloys, ZMA–0.19 Ge was the hardest, with the hardness decreasing with increasing Ge additions. The hardness of ZMA–Ge alloys decreases with the increase in Ge additions, with ZMA–1.8 Ge displaying an 18.78% reduction in hardness compared to ZMA–0 Ge.

In ZMA–0 Ge, a significant difference was observed between the nano hardness of the Zn phase and the eutectic phase, where the eutectic phase is 2.3 times harder compared to the Zn phase. The addition of 1.8 wt.% Ge decreased the hardness of the Zn phase of ZMA–0 Ge by 31.63%.

The addition of Ge into ZMA alloys was found to lead to an increase in the predicted ultimate tensile stress and yield stress values of the material up to 0.19 wt.%. However, this was followed by a decline in the strength-based properties when greater amounts of Ge were introduced.

Author Contributions: Conceptualisation, J.H.S. and D.J.P.; methodology, A.D.M., J.H.S., D.J.P., R.J.L. and E.S.; validation, A.D.M., J.H.S., D.J.P., R.J.L. and E.S.; formal analysis, A.D.M., J.H.S., D.J.P., R.J.L. and E.S.; investigation, A.D.M., J.H.S., D.J.P., R.J.L. and E.S.; resources, J.H.S. and D.J.P.; data curation, A.D.M., R.J.L. and E.S.; writing—original draft preparation, A.D.M.; writing—review and editing, A.D.M., J.H.S., D.J.P., R.J.L., P.B. and E.S.; visualisation, A.D.M., J.H.S., D.J.P., R.J.L. and E.S.; supervision, J.H.S., D.J.P. and P.B.; funding acquisition, J.H.S. and D.J.P. All authors have read and agreed to the published version of the manuscript.

Funding: The authors would like to thank EPSRC (Grant Code: EP/L015099/1) for funding via the COATED 2 Centre for Doctoral Training and WEFO-funded Materials & Manufacturing Academy (M2A) at Swansea University.

Institutional Review Board Statement: Not applicable.

Informed Consent Statement: Not applicable.

Data Availability Statement: The raw data supporting the conclusions of this article will be made available by the authors on request as the data also forms part of an ongoing study.

Acknowledgments: The authors would also like to acknowledge Tata Steel UK for providing the materials, and the MACH1 centre at Swansea University for use of their facilities to produce the experimental samples.

Conflicts of Interest: Author Peter Barker was employed by the company Tata Steel UK Limited. The remaining authors declare that the research was conducted in the absence of any commercial or financial relationships that could be construed as a potential conflict of interest.

References

1. Pola, A.; Tocci, M.; Goodwin, F.E. Review of Microstructures and Properties of Zinc Alloys. *Metals* **2020**, *10*, 253. [[CrossRef](#)]
2. Marder, A.R. The Metallurgy of Zinc-Coated Steel. *Prog. Mater. Sci.* **2000**, *45*, 191–271. [[CrossRef](#)]
3. Su, Y.; Fu, J.; Du, S.; Georgas, E.; Qin, Y.-X.; Zheng, Y.; Wang, Y.; Zhu, D. Biodegradable Zn–Sr Alloys with Enhanced Mechanical and Biocompatibility for Biomedical Applications. *Smart Mater. Med.* **2022**, *3*, 117–127. [[CrossRef](#)]
4. Shen, C.; Liu, X.; Fan, B.; Lan, P.; Zhou, F.; Li, X.; Wang, H.; Xiao, X.; Li, L.; Zhao, S.; et al. Mechanical Properties; In Vitro Degradation Behavior, Hemocompatibility and Cytotoxicity Evaluation of Zn-1.2Mg Alloy for Biodegradable Implants. *RSC Adv.* **2016**, *6*, 86410–86419. [[CrossRef](#)]
5. Gong, H.; Wang, K.; Strich, R.; Zhou, J.G. In Vitro Biodegradation Behavior, Mechanical Properties, and Cytotoxicity of Biodegradable Zn-Mg Alloy. *J. Biomed. Mater. Res.—Part B Appl. Biomater.* **2015**, *103*, 1632–1640. [[CrossRef](#)]
6. Li, H.; Yang, H.; Zheng, Y.; Zhou, F.; Qiu, K.; Wang, X. Design and Characterizations of Novel Biodegradable Ternary Zn-Based Alloys with IIA Nutrient Alloying Elements Mg, Ca and Sr. *Mater. Des.* **2015**, *83*, 95–102. [[CrossRef](#)]
7. Tong, X.; Zhang, D.; Zhang, X.; Su, Y.; Shi, Z.; Wang, K.; Lin, J.; Li, Y.; Lin, J.; Wen, C. Microstructure, Mechanical Properties, Biocompatibility, and in Vitro Corrosion and Degradation Behavior of a New Zn–5Ge Alloy for Biodegradable Implant Materials. *Acta Biomater.* **2018**, *82*, 197–204. [[CrossRef](#)]
8. Zhao, S.; Seitz, J.M.; Eifler, R.; Maier, H.J.; Guillory, R.J.; Earley, E.J.; Drelich, A.; Goldman, J.; Drelich, J.W. Zn-Li Alloy after Extrusion and Drawing: Structural, Mechanical Characterization, and Biodegradation in Abdominal Aorta of Rat. *Mater. Sci. Eng. C* **2017**, *76*, 301–312. [[CrossRef](#)]
9. Niu, J.; Tang, Z.; Huang, H.; Pei, J.; Zhang, H.; Yuan, G.; Ding, W. Research on a Zn-Cu Alloy as a Biodegradable Material for Potential Vascular Stents Application. *Mater. Sci. Eng. C* **2016**, *69*, 407–413. [[CrossRef](#)]
10. Tong, X.; Shi, Z.; Xu, L.; Lin, J.; Zhang, D.; Wang, K.; Li, Y.; Wen, C. Degradation Behavior, Cytotoxicity, Hemolysis, and Antibacterial Properties of Electro-Deposited Zn–Cu Metal Foams as Potential Biodegradable Bone Implants. *Acta Biomater.* **2020**, *102*, 481–492. [[CrossRef](#)]
11. Ahmadi, M.; Salgın, B.; Kooi, B.J.; Pei, Y. Cracking Behavior and Formability of Zn-Al-Mg Coatings: Understanding the Influence of Steel Substrates. *Mater. Des.* **2021**, *212*, 110215. [[CrossRef](#)]
12. Najafabadi, E.P.; Heidarpour, A.; Raina, S. Hot-Dip Galvanizing of High and Ultra-High Strength Thin-Walled CHS Steel Tubes: Mechanical Performance and Coating Characteristics. *Thin-Walled Struct.* **2021**, *164*, 107744. [[CrossRef](#)]
13. Ahmadi, M.; Salgın, B.; Kooi, B.J.; Pei, Y. The Effect of Grain Refinement on the Deformation and Cracking Resistance in Zn–Al–Mg Coatings. *Mater. Sci. Eng. A* **2022**, *840*, 142995. [[CrossRef](#)]
14. Schuerz, S.; Fleischanderl, M.; Luckeneder, G.H.; Preis, K.; Haunschmied, T.; Mori, G.; Kneissl, A.C. Corrosion Behaviour of Zn–Al–Mg Coated Steel Sheet in Sodium Chloride-Containing Environment. *Corros. Sci.* **2009**, *51*, 2355–2363. [[CrossRef](#)]
15. Prosek, T.; Larché, N.; Vlot, M.; Goodwin, F.; Thierry, D. Corrosion Performance of Zn–Al–Mg Coatings in Open and Confined Zones in Conditions Simulating Automotive Applications. *Mater. Corros.* **2010**, *61*, 412–420. [[CrossRef](#)]
16. De Bruycker, E.; Zermout, Z.; De Cooman, B.C. Zn-Al-Mg Coatings: Thermodynamic Analysis and Microstructure Related Properties. In *Materials Science Forum*; Trans Tech Publications Ltd.: Wollerau, Switzerland, 2007.
17. Persson, D.; Thierry, D.; LeBozec, N.; Prosek, T. In Situ Infrared Reflection Spectroscopy Studies of the Initial Atmospheric Corrosion of Zn-Al-Mg Coated Steel. *Corros. Sci.* **2013**, *72*, 54–63. [[CrossRef](#)]
18. Xu, M.; Han, D.; Zheng, Z.; Ma, R.; Du, A.; Fan, Y.; Zhao, X.; Cao, X. Effects of Cooling Rate on the Microstructure and Properties of Hot-Dipped Zn–Al–Mg Coatings. *Surf. Coat. Technol.* **2022**, *444*, 128665. [[CrossRef](#)]
19. Lee, J.-W.; Park, B.R.; Oh, S.-Y.; Yun, D.W.; Hwang, J.K.; Oh, M.-S.; Kim, S.J. Mechanistic Study on the Cut-Edge Corrosion Behaviors of Zn-Al-Mg Alloy Coated Steel Sheets in Chloride Containing Environments. *Corros. Sci.* **2019**, *160*, 108170. [[CrossRef](#)]
20. Wint, N.; Eaves, D.; Williams, G.; McMurray, H.N. The Effect of Composition and Thickness on the Mechanism and Kinetics of Filiform Corrosion Occurring on Zinc-Aluminium-Magnesium Coated Steel. *Corros. Sci.* **2021**, *179*, 109168. [[CrossRef](#)]
21. Prosek, T.; Hagström, J.; Persson, D.; Fuertes, N.; Lindberg, F.; Chocholatý, O.; Taxén, C.; Šerák, J.; Thierry, D. Effect of the Microstructure of Zn-Al and Zn-Al-Mg Model Alloys on Corrosion Stability. *Corros. Sci.* **2016**, *110*, 71–81. [[CrossRef](#)]
22. Prosek, T.; Nazarov, A.; Bexell, U.; Thierry, D.; Serak, J. Corrosion Mechanism of Model Zinc-Magnesium Alloys in Atmospheric Conditions. *Corros. Sci.* **2008**, *50*, 2216–2231. [[CrossRef](#)]
23. LeBozec, N.; Thierry, D.; Rohwerder, M.; Persson, D.; Luckeneder, G.; Luxem, L. Effect of Carbon Dioxide on the Atmospheric Corrosion of Zn-Mg-Al Coated Steel. *Corros. Sci.* **2013**, *74*, 379–386. [[CrossRef](#)]

24. Hammam, R.E.; Abdel-Gawad, S.A.; Moussa, M.E.; Shoeib, M.; El-Hadad, S. Study of Microstructure and Corrosion Behavior of Cast Zn–Al–Mg Alloys. *Int. J. Met.* **2023**, *17*, 2794–2807. [[CrossRef](#)]
25. Prosek, T.; Nazarov, A.; Goodwin, F.; Šerák, J.; Thierry, D. Improving Corrosion Stability of ZnAlMg by Alloying for Protection of Car Bodies. *Surf. Coat. Technol.* **2016**, *306*, 439–447. [[CrossRef](#)]
26. Zhang, M.; Zhou, G.; Sun, H.; Teng, X.; Zhao, Z. Effects of Ti and Zr Elements Addition on the Microstructure and Corrosion Resistance of Zn-2.5Al-2Mg Alloy. *Mater. Res. Express* **2020**, *7*, 026525. [[CrossRef](#)]
27. Gogola, P.; Gabalcová, Z.; Kusý, M.; Suchánek, H. The Effect of Sn Addition on Zn-Al-Mg Alloy; Part i: Microstructure and Phase Composition. *Materials* **2021**, *14*, 5404. [[CrossRef](#)] [[PubMed](#)]
28. Liu, G.; Teng, H.; Xu, C.; Shang, T.; Jiang, G.; Liu, Z. Influence of Si Contents on the Microstructure and Corrosion Resistance of the Zn-Al-Mg-Si Alloys. *Metall. Res. Technol.* **2024**, *121*, 201. [[CrossRef](#)]
29. Britton, D.A.; Penney, D.; Malla, A.D.; Mehraban, S.; Sullivan, J.; Goldsworthy, M.; McGettrick, J.; Johnston, R.; Mitchell, R.L.; Challinor, C. Effect of Antimony Additions on the Microstructure and Performance of Zn–Mg–Al Alloy Coatings. *NPJ Mater. Degrad.* **2024**, *8*, 62. [[CrossRef](#)]
30. Wint, N.; Malla, A.D.; Cooze, N.; Savill, T.; Mehraban, S.; Dunlop, T.; Sullivan, J.H.; Penney, D.; Williams, G.; McMurray, H.N. The Ability of Mg₂Ge Crystals to Behave as ‘Smart Release’ Inhibitors of the Aqueous Corrosion of Zn-Al-Mg Alloys. *Corros. Sci.* **2021**, *179*, 109091. [[CrossRef](#)]
31. Malla, A.D.; Sullivan, J.H.; Penney, D.J.; Dunlop, T.; Barker, P. Mechanistic Study on the Corrosion Behaviour of Zinc and Zinc-Calcium Alloys Designed for Enhanced Metallic Coatings in the Presence of Chloride and Phosphate Ions. *Corros. Sci.* **2023**, *213*, 110956. [[CrossRef](#)]
32. Oliver, W.C.; Pharr, G.M. An Improved Technique for Determining Hardness and Elastic Modulus Using Load and Displacement Sensing Indentation Experiments. *J. Mater. Res.* **1992**, *7*, 1564–1583. [[CrossRef](#)]
33. Oliver, W.C.; Pharr, G.M. Measurement of Hardness and Elastic Modulus by Instrumented Indentation: Advances in Understanding and Refinements to Methodology. *J. Mater. Res.* **2004**, *19*, 3–20. [[CrossRef](#)]
34. Pharr, G.M.; Oliver, W.C. Measurement of Thin Film Mechanical Properties Using Nanoindentation. *MRS Bull.* **1992**, *17*, 28–33. [[CrossRef](#)]
35. Kumar, K.S.; Van Swygenhoven, H.; Suresh, S. Mechanical Behavior of Nanocrystalline Metals and Alloys. *Acta Mater.* **2003**, *51*, 5743–5774. [[CrossRef](#)]
36. Cellini, F.; Gao, Y.; Riedo, E. Å-Indentation for Non-Destructive Elastic Moduli Measurements of Supported Ultra-Hard Ultra-Thin Films and Nanostructures. *Sci. Rep.* **2019**, *9*, 4075. [[CrossRef](#)] [[PubMed](#)]
37. Saha, R.; Nix, W.D. Effects of the Substrate on the Determination of Thin Film Mechanical Properties by Nanoindentation. *Acta Mater.* **2002**, *50*, 23–38. [[CrossRef](#)]
38. Rhee, H.; Lucas, J.P.; Subramanian, K.N. Micromechanical Characterization of Thermomechanically Fatigued Lead-Free Solder Joints. *J. Mater. Sci. Mater. Electron.* **2002**, *13*, 477–484. [[CrossRef](#)]
39. Chromik, R.R.; Vinci, R.P.; Allen, S.L.; Notis, M.R. Nanoindentation Measurements on Cu–Sn and Ag–Sn Intermetallics Formed in Pb-Free Solder Joints. *J. Mater. Res.* **2003**, *18*, 2251–2261. [[CrossRef](#)]
40. Frear, D.R.; Vianco, P.T. Intermetallic Growth and Mechanical Behavior of Low and High Melting Temperature Solder Alloys. *Metall. Mater. Trans. A* **1994**, *25*, 1509–1523. [[CrossRef](#)]
41. Rho, J.-Y.; Tsui, T.Y.; Pharr, G.M. Elastic Properties of Human Cortical and Trabecular Lamellar Bone Measured by Nanoindentation. *Biomaterials* **1997**, *18*, 1325–1330. [[CrossRef](#)]
42. Roos, W.H.; Wuite, G.J.L. Nanoindentation Studies Reveal Material Properties of Viruses. *Adv. Mater.* **2009**, *21*, 1187–1192. [[CrossRef](#)]
43. Lancaster, R.J.; Illsley, H.W.; Davies, G.R.; Jeffs, S.P.; Baxter, G.J. Modelling the Small Punch Tensile Behaviour of an Aerospace Alloy. *Mater. Sci. Technol.* **2017**, *33*, 1065–1073. [[CrossRef](#)]
44. Matocha, K. Small-Punch Testing for Tensile and Fracture Behavior: Experiences and Way Forward. In *Small Specimen Test Techniques: 6th Volume*; ASTM International: West Conshohocken, PA, USA, 2015; pp. 1–15, ISBN 9780803175976.
45. Bruchhausen, M.; Holmström, S.; Simonovski, I.; Austin, T.; Lapetite, J.-M.; Ripplinger, S.; de Haan, F. Recent Developments in Small Punch Testing: Tensile Properties and DBTT. *Theor. Appl. Fract. Mech.* **2016**, *86*, 2–10. [[CrossRef](#)]
46. Moreno, M.F.; Bertolino, G.; Yawny, A. The Significance of Specimen Displacement Definition on the Mechanical Properties Derived from Small Punch Test. *Mater. Des.* **2016**, *95*, 623–631. [[CrossRef](#)]
47. Mao, X.; Takahashi, H. Development of a Further-Miniaturized Specimen of 3 Mm Diameter for Tem Disk (ø 3 Mm) Small Punch Tests. *J. Nucl. Mater.* **1987**, *150*, 42–52. [[CrossRef](#)]
48. Cao, X.; Zhou, X.; Li, Z.; Luo, Z.; Duan, J. Interface Microstructure and Nanoindentation Characterization of Laser Offset Welded 5052 Aluminum to Press-Hardened Steel Using a Brass Interlayer. *Metals* **2019**, *9*, 1143. [[CrossRef](#)]
49. Lancaster, R.J.; Jeffs, S.P.; Haigh, B.J.; Barnard, N.C. Derivation of Material Properties Using Small Punch and Shear Punch Test Methods. *Mater. Des.* **2022**, *215*, 110473. [[CrossRef](#)]
50. Yao, C.; Lv, H.; Zhu, T.; Zheng, W.; Yuan, X.; Gao, W. Effect of Mg Content on Microstructure and Corrosion Behavior of Hot Dipped Zn–Al–Mg Coatings. *J. Alloys Compd.* **2016**, *670*, 239–248. [[CrossRef](#)]

51. Jin, H.; Zhao, S.; Guillory, R.; Bowen, P.K.; Yin, Z.; Griebel, A.; Schaffer, J.; Earley, E.J.; Goldman, J.; Drelich, J.W. Novel High-Strength, Low-Alloys Zn-Mg (<0.1 Wt% Mg) and Their Arterial Biodegradation. *Mater. Sci. Eng. C* **2018**, *84*, 67–79. [[CrossRef](#)]
52. Drápala, J.; Kostiuková, G.; Losertová, M. Contribution to the Aluminum–Tin–Zinc Ternary System. *IOP Conf. Ser. Mater. Sci. Eng.* **2017**, *266*, 012002. [[CrossRef](#)]

Disclaimer/Publisher’s Note: The statements, opinions and data contained in all publications are solely those of the individual author(s) and contributor(s) and not of MDPI and/or the editor(s). MDPI and/or the editor(s) disclaim responsibility for any injury to people or property resulting from any ideas, methods, instructions or products referred to in the content.